Results in Physics 40 (2022) 105869

Contents lists available at ScienceDirect

Results in Physics

journal homepage: www.elsevier.com/locate/rinp

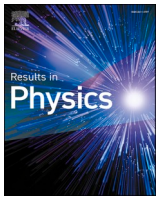

Surface symmetry determination by a deep learning application of optical second-harmonic generation results

D.G. Jeong, J.S. Lee *

Department of Physics and Photon Science, Gwangju Institute of Science and Technology (GIST), Gwangju 61005, Korea

ARTICLE INFO

Keywords:
Second-harmonic generation
Deep learning
Surface and interface symmetry characterization
Point group symmetry discrimination
Sequence data analysis

ABSTRACT

Optical second-harmonic generation (SHG) technique is widely used to characterize the structural symmetry of condensed matters not only for the bulk but also for the surface states. Since experimental results of the SHG anisotropy patterns often contain multiple contributions from bulk and surface states, a conventional regression process may not provide a unique solution about the symmetry of each part. With a given symmetry for the bulk state, we here develop a discriminator for the surface symmetry by exploiting neural architectures based on 1D convolution layers where simulation results of SHG anisotropy patterns are taken as learning sequence data. Since SHG experimental results have limited information for determining a unique symmetry out of several symmetry candidates, our discriminator consists of tens of neural architectures optimized with different hyperparameters. As a final output, the surface symmetry discriminator gives a weighted sum of results suggested from all the individual neural architectures. We demonstrate that the discrimination results of the deep learning approach agree well with those of the conventional regression method for GaAs and Bi_2Se_3.

A precise characterization of structural symmetry is essential in solid-state material researches. The bulk crystalline symmetry can be determined with well-established diffraction techniques using X-ray, neutron, and electron beams. The optical second-harmonic generation (SHG) is also a powerful tool in characterizing the bulk symmetry, and has been widely used to investigate polar, ferroelectric, and multiferroic states [1–4]. Furthermore, the technique is particularly useful in characterizing the surface and interface symmetry since the SHG process is primarily allowed in the non-centrosymmetric state, which is naturally realized at such structural boundaries [2]. By the way, the as the optical beam can easily penetrate into the inner part of the bulk, there are often multiple contributions to the SHG responses which arise not only from the surface but also from the bulk. Whereas non-centrosymmetric materials endow the bulk electric dipole contribution, centrosymmetric materials also can have the bulk contribution from the electric quadrupole [5]. Therefore, it is a challenging task to determine the additional symmetry of the surface and/or the interface based on the SHG responses which contain multiple contributions from both bulk and surface of the given sample. In analyzing the SHG results, many conventional optimization techniques are usually adopted to optimize a large number of tensor components involved with multiple SHG contributions. By the way, such techniques require much effort to overcome the so-called local minimum problem and consume much time by having trials and errors with a wide range of initial tensor components. Even if one of the fitting conditions would be successfully obtained, one should further check whether the other symmetry combinations may account for the experiment results. In this respect, it is worth to try an alternative approach for the SHG result analyses.

Recently, the deep learning methodology has been widely applied to the solid-state materials science [6], and it is proved to be useful in discriminating the system's status which is described by sequence data [7]. For example, Lee *et al.* took X-ray diffraction patterns as the sequence data for the convolution neural architecture, and demonstrated that structural phase of complex inorganic compounds can be successfully classified with the machine learning technique [8]. Our problem is similar to this case. SHG anisotropy patterns are obtained experimentally with a variation of an azimuth angle of the sample, and such sequence data in the azimuth angle dimension contain essential information of the sample symmetry. While the structural symmetry may be determined simply by the conventional fitting analysis, namely by comparing such results with a prediction based on a certain symmetry, the deep learning approach for the sequence data can be also advantageous in solving the symmetry discrimination problem based on the SHG measurement.

* Corresponding author.
E-mail address: jsl@gist.ac.kr (J.S. Lee).

https://doi.org/10.1016/j.rinp.2022.105869
Received 16 May 2022; Received in revised form 18 July 2022; Accepted 30 July 2022
Available online 3 August 2022

In this work, we develop a surface symmetry discriminator by exploiting the model-driven deep learning approach. We organize training data sets using a well-defined susceptibility model for several symmetry candidates. The ADAM solver optimizes neural parameters of 1D convolution-based architectures [9]. When each optimization process is running, several sets of hyperparameters are chosen with a Bayesian optimization solver which tries 30 iterations. We collect approximately 10 optimized results having the validation score near the best, and use these results for statistical inferencing of the additional symmetry. We confirm that the inference results are reasonable in discriminating the surface symmetry for GaAs (001) and Bi_2Se_3 (0001).

Fig. 1 displays the conventional experimental geometry of the SHG measurement. Laser pulses irradiate the sample with an incidence angle $\theta_{\text{in}} = 45^{\circ}$, and the intensity of second-harmonic wave generated from the sample is monitored with a variation of the azimuth angle φ_{azi}. There are four polarization combinations for fundamental and second-harmonic waves, namely, PP, PS, SP, and SS, where the first and the second letters denote *p*- or *s*-polarization states of fundamental and second-harmonic waves, respectively. Fig. 1(b) displays the rotational anisotropy patterns of the SHG intensity for GaAs and Bi_2Se_3. For the (001)-oriented GaAs, we took the results using the femtosecond laser with a repetition rate 80 MHz as described in Ref. [10]. For Bi_2Se_3, oriented along (0001) in the hexagonal convention, the results are taken from Ref. [11]. The results for GaAs and Bi_2Se_3 are given to be fourfold-like and threefold-like, which reflect $\bar{4}3m$ and $\bar{3}m$ point group symmetry for GaAs and Bi_2Se_3, respectively (Fig. 2).

In calculating the SHG intensity as a function of the sample azimuth, we first define the input electric field of the fundamental wave inside the crystal which is originally *p*- or *s*-polarized. The outgoing second harmonic wave is defined inside the crystal following the induced second harmonic polarization, and its *p*- or *s*-polarization component is selected outside the crystal. In all these processes, Fresnel coefficients are appropriately adopted following the convention introduced in the previous work by Mizrahi and Sipe [12]. In understanding SHG responses presented in Fig. 1(b), we consider three different SHG sources which are assumed to contribute to the final signal incoherently as

$$I_i^{2\omega} \propto \left[\chi_{ijk}^{(2)} E_j^{\omega} E_k^{\omega}\right]_{\text{ED}}^2 + \left[\chi_{ijkl}^{(3)} \partial_j E_k^{\omega} E_l^{\omega}\right]_{\text{EQ}}^2 + \left[\chi_{ijk}^{(2)} E_j^{\omega} E_k^{\omega}\right]_{\text{sED,}}^2 \quad (1)$$

where the contributions from bulk electric dipole (ED), bulk electric quadrupole (EQ), and surface electric dipole (sED) are given in order. Although the coherent summation of multiple contributions may be adopted, the incoherent summation explains the experimental results better particularly for Bi_2Se_3. We take second- and third-order susceptibilities as free variables which allow the dimensional match between different terms and also include the role of different proportional coefficients. As aforementioned, our goal is to determine the structural symmetry for the surface/interface from the SHG results containing such multiple contributions, and it can be achieved by referring solely to the surface contribution irrespective of its relative strength with respect to the bulk contribution.

We now explain the deep learning architecture prepared for the additional symmetry discrimination. For the given bulk symmetry, additional symmetry candidates for the surface are selected from hierarchically lower symmetries within two-level than the bulk one. To enhance the performance of the discriminator, we introduce 10 features for sequence data. The normalized SHG model outputs are first generated by equation (1) with random susceptibility tensor components for four polarization states PP, PS, SP, and SS. Additionally, the first derivatives of such outputs are also considered as they may focus more on SHG signals without constant contributions, which can arise easily from the bulk quadrupole. Whereas we consider a Fresnel coefficient correction with random refractive index values 1 – 6 for fundamental and second harmonic waves [12], two additional features are prepared with random stepwise sequences based on refractive index values. They help to secure the symmetry learning with a less sensitivity to the uncertainty in the refractive index. All together, we prepared approximately 5×10^4 input data sets for the given symmetry tag, where a single data set is composed of azimuth-dependent data for aforementioned 10 features. For each data point, we consider experimental uncertainties by including a random incidence angle error of $\pm 2^{\circ}$ and random modifications of output amplitudes by $\pm 2.5\%$.

A Bayesian optimization algorithm was introduced to optimize the neural architecture suitable for our desired problem. The algorithm tries the deep learning process 30 times with L^1 penalization. For this, the objective function value Z is defined as $Z = 1 - C$, where the correctness C measures the similarity between the deep learning estimation and actual results, and it ranges from 0 to 1. It finds the best configuration of the neural architecture with a minimal Z by adjusting section width, initial learning rate, L^2 regularization factor, and dropout rate. Once the hyperparameters are fixed, the ADAM solver runs to fit neural parameters of the architecture for generating the same categorical estimation

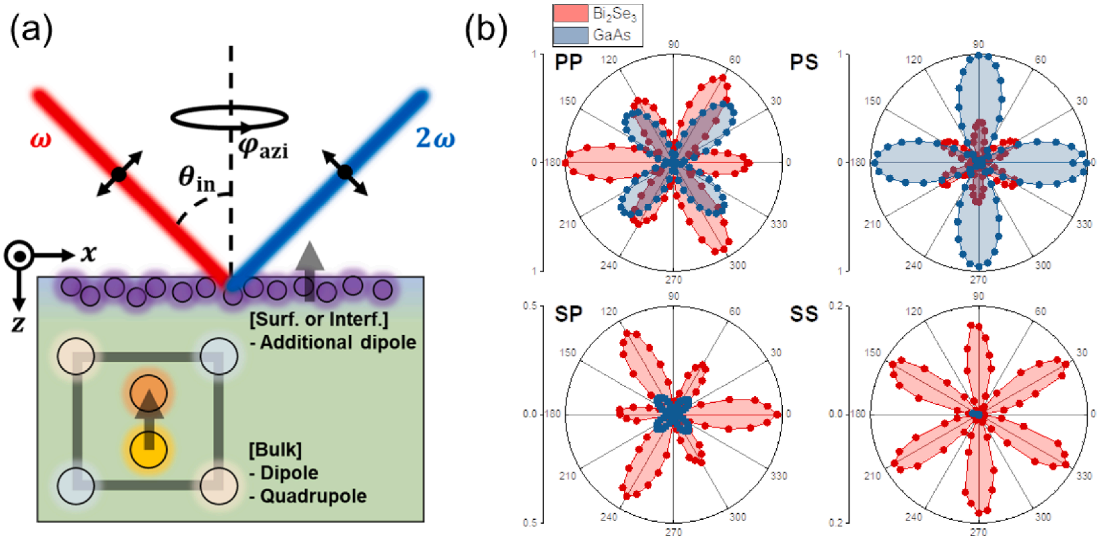

Fig. 1. (a) Schematic for the optical second-harmonic generation (SHG) experiment. The fundamental wave is incident on the sample with an incidence angle θ_{in}, and the second-harmonic wave is monitored in a reflection geometry with a variation of the sample azimuth φ_{azi}. The SHG process is allowed from the inner bulk and the interface in terms of electric dipole and electric quadrupole. (b) Rotation anisotropy patterns of the SHG intensity for GaAs and Bi_2Se_3. The crystals are oriented along (001) and (0001) directions, respectively. The results for Bi_2Se_3 are taken from Ref. [11].

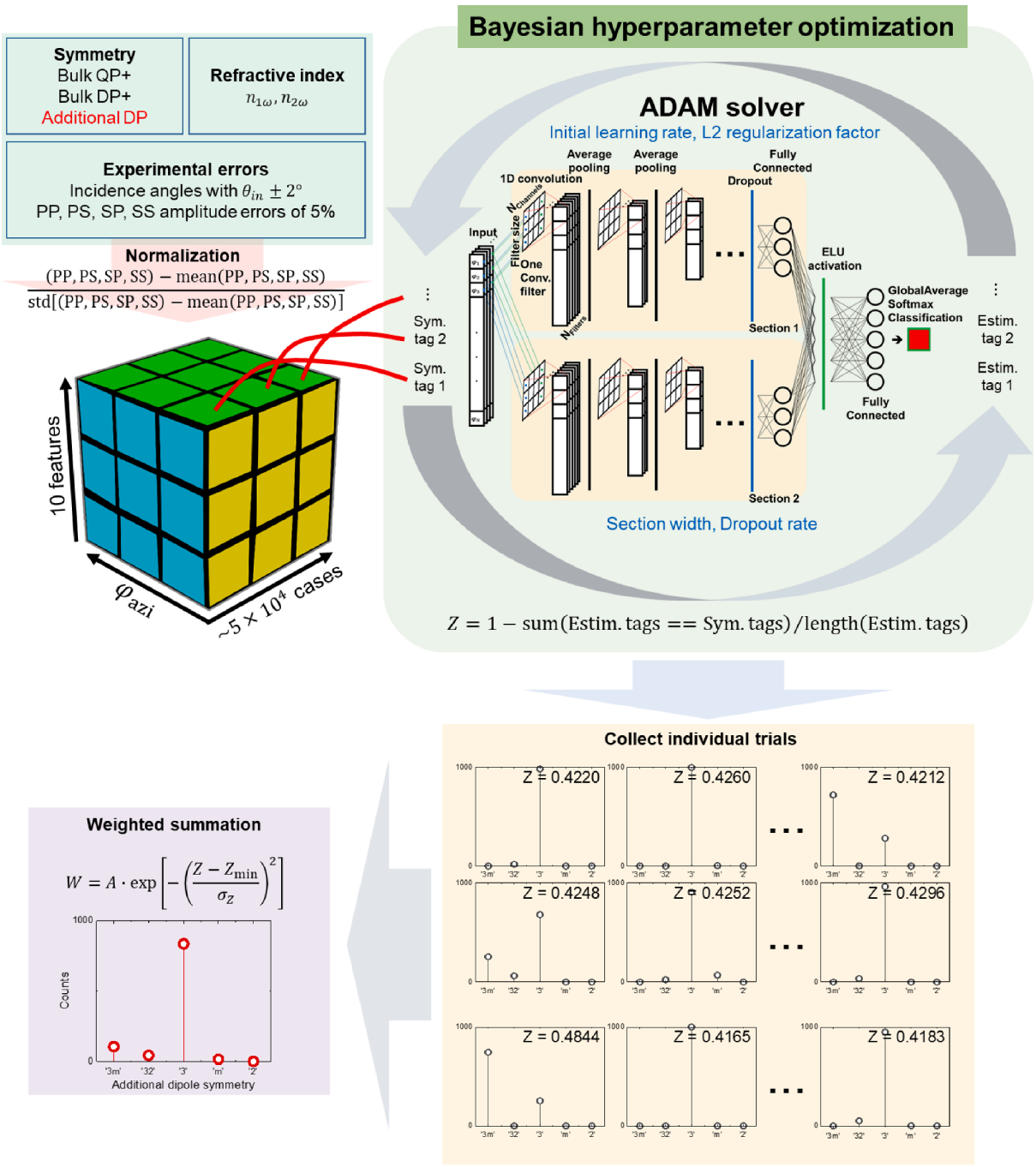

Fig. 2. Overall flow of deep learning process in this work. For the given structural symmetry of the bulk state, symmetry candidates of the surface are selected from hierarchically-two-level lower symmetry species, and azimuth-dependent SHG results are generated with randomly chosen susceptibility tensor components. Hyperparameters are optimized by the Bayesian optimization algorithm in total 30 iteration runs. Several neural architectures optimized with different hyperparameters give individual discrimination results, and our discriminator shows the inference result as a weighted summation of the whole suggestions.

results with input symmetry tags. With these processes, we could avoid both under- and over-fitting results by making the neural architecture have the comparable complexity to our problem.

When we took discrimination results from each neural architecture, we generated 1000 inputs by adding Gaussian random fluctuation error in original experiment data, and collected the counts that each architecture indicates. By the way, we observe that one neural architecture suggests only a single symmetry candidate, and the other architectures suggest different symmetries. We attribute this observation to the possible existence of many local minima. Also, it may be attributed to insufficient information of the usual SHG experiment to determine the symmetry of the additional dipole as the experimental result may reflect only some parts of susceptibility tensors [2,13]. To avoid this technical problem, we use the L^1 penalization in the Bayesian optimization which leads to various objective function results Z that should be minimized with the L^1 norm, and hence to several best configurations of hyperparameters. From each neural architecture optimized with different starting hyperparameters, we collected the count distribution with the randomly perturbed 1000 inputs. Finally, we determined our discrimination result by applying a Gaussian weighted summation of each result according to the Z values.

We now demonstrate the application results of our surface symmetry

discriminator for GaAs, which is one of the most representative polar semiconductors. GaAs has a zinc blende crystalline structure, and its point group symmetry is $\bar{4}3m$. Since it is non-centrosymmetric, we consider first the electric dipole contribution from the bulk. By the way, we exclude the contribution from the bulk quadrupole as it is usually much weaker than the bulk ED contribution. We additionally consider a possible contribution from the surface, of which point group symmetry is supposed to be unknown and hence to be determined. From the symmetry $\bar{4}3m$, there are primarially six symmetry subgroups, namely, 23, $\bar{4}2m$, $\bar{4}$, mm2, 222, and 3 which are hierarchically lower within the two-level as listed in Fig. 3(a). Therefore, the final learning symmetry tags are $\bar{4}3m(ED) + 23(sED)$, $\bar{4}3m(ED) + \bar{4}2m(sED)$, $\bar{4}3m(ED) + 3\,m$ (sED), $\bar{4}3m(ED) + \bar{4}(sED)$, $\bar{4}3m(ED) + mm2(sED)$, $\bar{4}3m(ED) + 222(sED)$ and $\bar{4}3m(ED) + 3(sED)$. We consider also an additional symmetry tag of $\bar{4}3m(ED) + \bar{4}3m(sED)$ supposing that the surface structural symmetry would remain the same as the bulk one. Before discussing the deep learning results, we check how well each symmetry tag would explain the experimental results based on the conventional fitting analysis. Fig. 3(b) displays that the additional consideration of mm2 can fit the experimental results reasonably well. Actually, there are mainly four symmetries that give comparable fitting qualities; as shown in Fig. 3(c), R^2 is given to be almost unity when $\bar{4}2m$, $\bar{4}$, mm2, and 222 are considered for the surface symmetry. Interestingly, the symmetry groups of 23, $\bar{4}3m$, and 3 containing threefold rotation operations fail to fit the experimental results.

Now we examine discrimination results for the additional symmetry based on our neural architecture for GaAs. As aforementioned, we have considered several different hyperparameter sets which have their own optimized neural architecture. Small dots in Fig. 3(d) display the final counts from such individual neural architecture. These small dots are largely distributed for four additional dipole symmetries of $\bar{4}2m$, $\bar{4}$, mm2, and 222 indicating that different neural architectures can give different suggestions. The large open symbols are weighted counts obtained by considering all the suggestions. Interestingly, these four symmetries having the meaningful suggestions are in good agreements with symmetries having the large R^2 shown in Fig. 3(b). This confirms that the neural architecture designed here works well to discriminate the additional dipole symmetry for GaAs.

It should be noted that these mathematical approaches of the fitting analysis and the deep learning do not simply suggest a unique symmetry for the GaAs surface state. This is partly because information provided by the SHG measurement is not enough. Since only some parts of the whole tensor components are involved for the experimental results, different symmetry tags can produce similar anisotropy patterns. To improve the discrimination efficiency, it would be helpful to collect more information, for example, with different incidence angles. Also, it is a good strategy to consider the actual physical circumstance of the target crystal. In this specific case of GaAs, we can safely suppose that the additional ED contribution to the SHG process originates from the surface where the fourfold rotational symmetry is often broken by forming, for example, a (2×4) surface reconstruction [14]. We therefore exclude symmetries $\bar{4}2m$ and $\bar{4}$ from the surface symmetry candidates. Between mm2 and 222, although the symmetry mm2 is usually suggested for the surface symmetry of GaAs by considering the surface band bending [15], the symmetry 222 may not be excluded if only SHG results are considered.

We now move on to the second example about Bi_2Se_3. As one of the most famous topological insulators, there have been several SHG reports characterizing the surface symmetry, which is directly connected to the topological surface state [16]. Because the bulk symmetry is $\bar{3}m$ which is centrosymmetric, we first consider the bulk EQ contribution. And, the candidates for the surface symmetry is chosen from the hierarchically lower symmetries within the two-level, namely $2/m$, $3m$, 32, $\bar{3}$, 3, m, and 2, as displayed in Fig. 4(a). Among them, we exclude $\bar{3}$ and $2/m$ from the surface symmetry candidates for the SHG source since they are centrosymmetric. Therefore, the final learning symmetry tags are $\bar{3}m(EQ) + 3m(sED)$, $\bar{3}m(EQ) + 32(sED)$, $\bar{3}(EQ) + m(sED)$, $\bar{3}m(EQ) +$

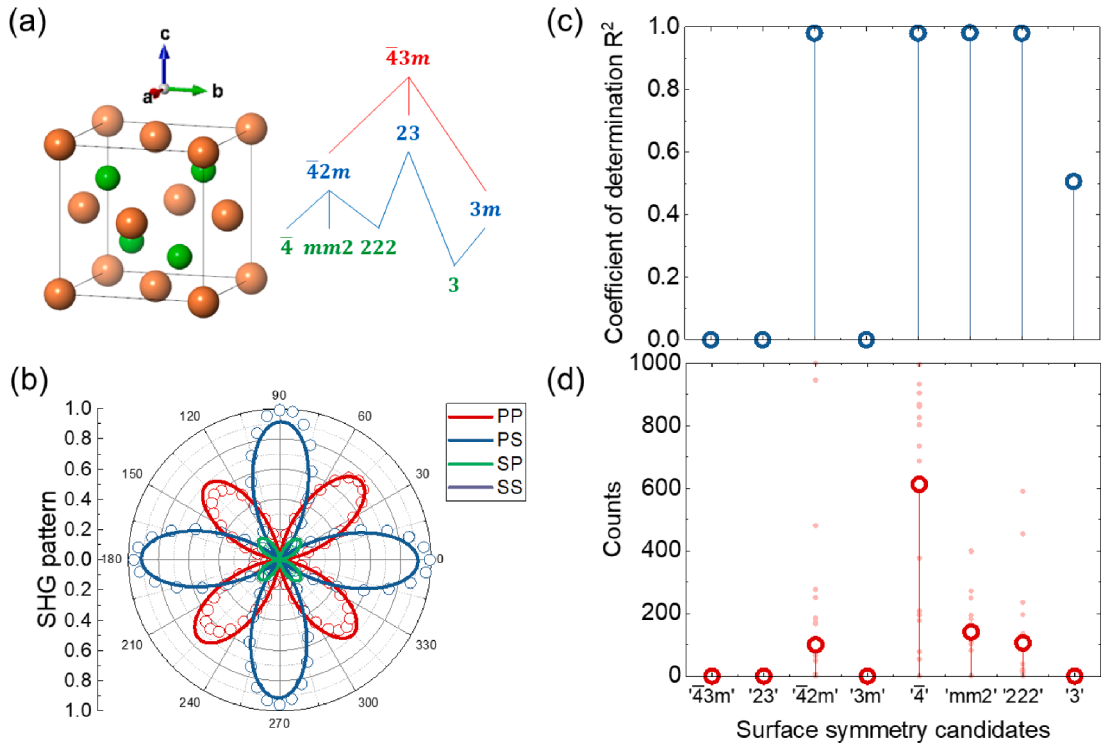

Fig. 3. Symmetry discrimination result for the surface states of GaAs(001). (a) The point group symmetry hierarchy from $\bar{4}3\mathbf{m}$, the symmetry of bulk GaAs. (b) Regression results obtained by considering contributions from the bulk $\bar{4}3\mathbf{m}$ and the surface mm2 symmetry. (c) Coefficient of determination from the conventional regression method for several symmetry candidates of the GaAs interface state. (d) Discrimination results for the surface symmetry of GaAs.

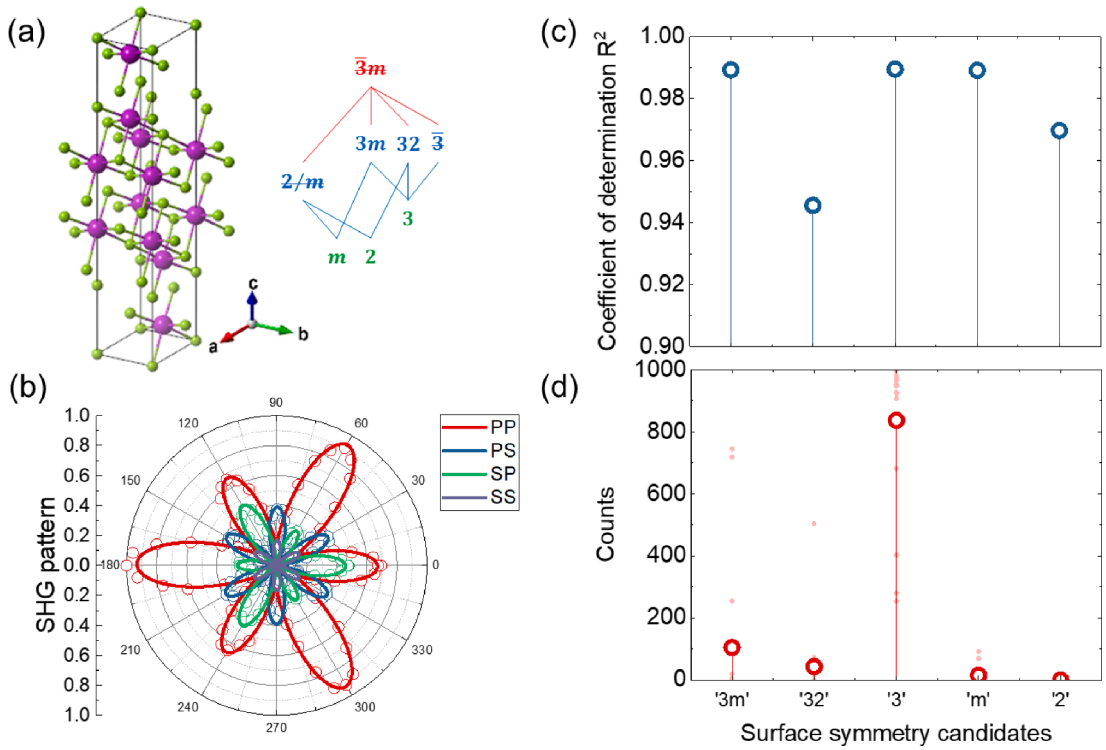

Fig. 4. Symmetry discrimination result for the surface states of Bi_2Se_3(0001). (a) The point group symmetry hierarchy from $\bar{3}$**m**, the bulk symmetry of Bi_2Se_3. The symmetries $\bar{3}$**m** and 2/**m** are excluded as they are centrosymmetric and hence has no electric dipole contribution to the SHG response. (b) Regression results obtained by considering contributions from the bulk $\bar{3}$**m** and the surface 3**m** symmetry. (c) Coefficient of determination from the conventional regression method for several symmetry candidates of the Bi_2Se_3 interface state. (d) Discrimination results for the surface symmetry of Bi_2Se_3.

2(sED), and $\bar{3}$m(EQ) + 3(sED). An example of the conventional regression results is shown in Fig. 4(b) for the symmetry tag $\bar{3}$m(QP) + 3m(DP). The coefficient of determination displayed in Fig. 4(c) are comparable for all the five symmetry tags, which means the SHG experimental system intrinsically has insufficient information to determine the surface symmetry.

Fig. 4(d) displays the discrimination result from the neural architectures optimized for the bulk $\bar{3}$m symmetry. Within the first-lower-level symmetries, namely 3m and 32, the symmetry 3 m has the higher suggestion. Actually, the symmetry 3 m has often been assigned to the surface symmetry of Bi_2Se_3 [11]; as Se ions easily escape from the surface, their vacancy can develop the surface band bending, and hence lead to the 3 m surface symmetry. Extending the symmetry candidate to the second-lower-level, it is found that the symmetry 3 has the much higher suggestion. The higher count for the symmetry 3 compared to 3 m is understood from their hierarchy relationship; the symmetry 3 has naturally higher degrees of freedom in tensor components than 3 m. Although 3 m is usually referred to the surface symmetry of Bi_2Se_3 [11], a possibility to have the surface symmetry 3 would not be excluded provided that only the SHG results are considered.

In summary, we developed a discriminator for the point group symmetry of surface states by using a model-driven deep learning technique for azimuth-dependent SHG anisotropy patterns. It should be noted that experimental results are sensitive to only some parts of the whole nonlinear susceptibility tensor components, and the hierarchically lower symmetries have a higher degree of freedom of nonzero tensor components. Namely, the model has insufficient information to exactly determine the additional symmetry. To overcome this limitation, we introduced statistical inference for the discrimination process. When the Bayesian optimization was performed for hyperparameters of the neural architecture, we used L^1 penalization which allows to have several best sets of hyperparameters. Then we collected discrimination results of each optimized architecture, and applied statistical inference with Gaussian weighted summation based on the penalization score. We demonstrated the discrimination results of two representative examples of GaAs and Bi_2Se_3, where the surface symmetry candidates are properly suggested. The advantages of the deep learning approach in analyzing SHG results are (i) to discriminate crystal symmetries very fast (within seconds), (ii) to avoid the local minimum problem by taking the statistical approach, and (iii) to secure a generality about symmetry candidates as they are described by a probability distribution. The symmetry discriminator demonstrated in this work can be helpful in assigning the point group symmetries for the hidden layers of surfaces and interfaces, which can be a complementary approach to the conventional regression method and also a firm basis for the further fundamental and application researches exploiting surface sciences.

CRediT authorship contribution statement

D.G. Jeong: Conceptualization, Methodology, Software, Validation, Formal analysis, Investigation, Data curation, Writing – original draft, Writing – review & editing, Visualization. **J.S. Lee:** Conceptualization, Supervision, Project administration, Visualization, Writing – original draft, Writing – review & editing.

Declaration of Competing Interest

The authors declare that they have no known competing financial interests or personal relationships that could have appeared to influence the work reported in this paper.

Data availability

Data will be made available on request.

References

[1] Fiebig M, Pavlov VV, Pisarev RV. Second-harmonic generation as a tool for studying electronic and magnetic structures of crystals. JOSA B 2005;22(1):96–118. https://doi.org/10.1364/JOSAB.22.000096.

[2] Roh CJ, Jung M-C, Kim JR, Go K-J, Kim J, Oh HJ, et al. Polar metal phase induced by oxygen octahedral network relaxation in oxide thin films. Small 2020;16(40):2003055.

[3] Ju H, Lee Y, Kim KT, Choi IH, Roh CJ, Son S, et al. Possible persistence of multiferroic order down to bilayer limit of van der Waals material NiI_2. Nano Lett 2021;21(12):5126–32. https://doi.org/10.1021/acs.nanolett.1c01095.

[4] Roh CJ, Hamh SY, Woo CS, Kim KE, Yang CH, Lee JS. Ferroelectric domain states of a tetragonal $BiFeO_3$ thin film investigated by second harmonic generation microscopy. Nanoscale Res Lett 2017;12(1):1–6. https://doi.org/10.1186/s11671-017-2126-5.

[5] Torchinsky DH, Chu H, Zhao L, Perkins NB, Sizyuk Y, Qi T, et al. Structural distortion-induced magnetoelastic locking in Sr_2IrO_4 revealed through nonlinear optical harmonic generation. Phys Rev Lett 2015;114(9):096404. https://doi.org/10.1103/PhysRevLett.114.096404.

[6] Schmidt J, Marques MRG, Botti S, Marques MAL. Recent advances and applications of machine learning in solid-state materials science. npj Comput Mater 2019;5(1).

[7] Azari AR, Lockhart JW, Liemohn MW, Jia X. Incorporating physical knowledge into machine learning for planetary space physics. Front Astron Space Sci 2020;7. https://doi.org/10.3389/fspas.2020.00036.

[8] Lee JW, Park WB, Lee JH, Singh SP, Sohn KS. A deep-learning technique for phase identification in multiphase inorganic compounds using synthetic XRD powder patterns. Nat Commun 2020;11(1):1–11. https://doi.org/10.1038/s41467-019-13749-3.

[9] Mendolia I, Contino S, Perricone U, Ardizzone E, Pirrone R. Convolutional architectures for virtual screening. BMC Bioinf 2020;21(8):1–14. https://doi.org/10.1186/s12859-020-03645-9.

[10] Choi IH, Kim MS, Kang C, Lee JS. Ultrafast real-time tracing of surface electric field generated via hot electron transport in polar semiconductors. Appl Surf Sci 2022;571:151279. https://doi.org/10.1016/j.apsusc.2021.151279.

[11] Mclver JW, Hsieh D, Drapcho SG, Torchinsky DH, Gardner DR, Lee YS, et al. Theoretical and experimental study of second harmonic generation from the surface of the topological insulator Bi_2Se_3. Phys Rev B 2012;86(3):035327. https://doi.org/10.1103/PhysRevB.86.035327.

[12] Mizrahi V, Sipe JE. Phenomenological treatment of surface second-harmonic generation. JOSA B 1988;5(3):660–7. https://doi.org/10.1364/JOSAB.5.000660.

[13] Roh CJ, Kim JR, Park S, Shin YJ, Yang BJ, Noh TW, et al. Structural symmetry evolution in surface and interface of $SrRuO_3$ thin films. Appl Surf Sci 2021;553:149574. https://doi.org/10.1016/j.apsusc.2021.149574.

[14] Ohtake A. Surface reconstructions on GaAs (001). Surf Sci Rep 2008;63(7):295–327. https://doi.org/10.1016/j.surfrep.2008.03.001.

[15] Qi J, Yeganeh MS, Koltover I, Yodh AG, Theis WM. Depletion-electric-field-induced changes in second-harmonic generation from GaAs. Phys Rev Lett 1993;71(4):633. https://doi.org/10.1103/PhysRevLett.71.633.

[16] Hamh SY, Park SH, Jerng SK, Jeon JH, Chun SH, Jeon JH, et al. Surface and interface states of Bi_2Se_3 thin films investigated by optical second-harmonic generation and terahertz emission. Appl Phys Lett 2016;108(5):051609. https://doi.org/10.1063/1.4941420.